Room-Temperature Activation of CO2 by Dual Defect-Stabilized Nanoscale Hematite ($Fe_{2-\delta}O_{3-v}$): Concurrent Role of Fe and O Vacancies

Divya Nagaraju,*[‡] Sharad Gupta,[‡] Deepak Kumar,[‡] Chamundi P. Jijil,[‡] Suresh k. Bhat,[‡] Dinesh Jagadeesan,*[‡,§] and Satishchandra Ogale*[‡,†]

[†]Department of Physics and Centre for Energy Science, Indian Institute of Science Education, Research, Pashan, 411008 Pune, India
[‡]CSIR-National Chemical Laboratory, Pashan, 411008 Pune, India
[§]Indian Institute of Technology, Palakkad, 678557 Kerala, India

S Supporting Information

ABSTRACT: We demonstrate that synthetically controlled concurrent stabilization of Fe and O vacancy defects on the surface of interbraided nanoscale hematite ($Fe_{2-\delta}O_{3-v}$) renders an interesting surface chemistry which can reduce CO_2 to CO at room temperature (RT). Importantly, we realized a highly enhanced output of 410 μmol h^{-1} g^{-1} at RT, as compared to that of 10 μmol h^{-1} g^{-1} for bulk hematite. It is argued based on the activity degradation under cycling and first principles density functional theory calculations that the excess chemical energy embedded in the defect-stabilized surface is expended in this high-energy conversion process, which leads to progressive filling up of oxygen vacancies.
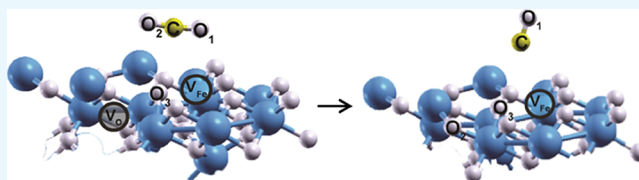
INTRODUCTION

One of the possible grand designs for alleviating the concentration of atmospheric CO_2 is to adsorb and chemically convert it into useful products.[1−3] The critical bottleneck still lies in the thermodynamic stability of CO_2[4−6] which necessitates an input of impractically high amount of energy ($CO_2 \rightarrow CO + 1/2O_2$, ΔG_{1000K} = 190.5 kJ mol^{-1}) or reducing agent such as H_2 for its activation.[7−9] Activation essentially involves transfer of electrons to the antibonding orbitals of CO_2 and converting its linear structure to a bent anion radical $CO_2^{\delta-}$.[10] It has been shown that alkaline earth metals and metal oxides can effectively chemisorb CO_2 by forming an anion radical on the surface.[11−13] Further, decomposition of surface $CO_2^{\delta-}$ to CO has been reported on transition metals with low work function.[14−17] Recently, Toda et al. have discussed the interesting possibility of room-temperature (RT) dissociation of CO_2 to CO.[18] Also, there are a few works on gas-phase activation and reduction of CO_2 to CO on defect oxide surfaces in dark at RT and further the enhanced increase in CO production upon light irradiation.[19,20]

As the challenge of tackling large volumes of CO_2 is intensifying, there is a growing interest to develop new materials that can activate CO_2 at lower temperatures and study the nature of the attendant interaction. It is envisaged that such studies may provide crucial insights into the nature of the active sites that may be rationally developed to produce robust systems for high volume applications. From this perspective, we demonstrate herein an interesting case of RT activation of CO_2 on the surface of dual defect-stabilized nanoscale hematite (DSNH), which provides the sufficiently required electron-rich sites. Importantly, we did not use any reductants such as H_2 in the studies yet realized a very impressive conversion output of 410 μmol h^{-1} g^{-1} at RT as compared to the output of a mere 10 μmol h^{-1} g^{-1} for the bulk hematite (BH) powder in a flow reactor. On the basis of the observation of activity decay with cycling and first principles density functional theory (DFT) calculations, it is argued that the excess chemical energy embedded in the dual defect-stabilized surface is expended in this high-energy conversion process, which leads to progressive filling up of oxygen vacancies.

RESULTS AND DISCUSSION

The material was synthesized by the metalloaerogel pyrolysis method (Scheme S1 in the Supporting Information). The porous MOF-100 aerogel after freeze-drying is seen to be transformed into a highly mesoporous, layered, and three-dimensional (3D) interbraided-type architecture (Figure 1a,b) upon the controlled two-step pyrolysis employed in the synthesis. From the transmission electron microscopy (TEM) image (Figure 1b) of our DSNH, it is evident that the material has a uniform particle size distribution with sizes between 18 and 25 nm.

The powder X-ray diffraction (PXRD) patterns (Figure 1c) of BH and DSNH match well with the standard pattern of hematite (JCPDS card no. 33 0664), belonging to the $R\bar{3}c$
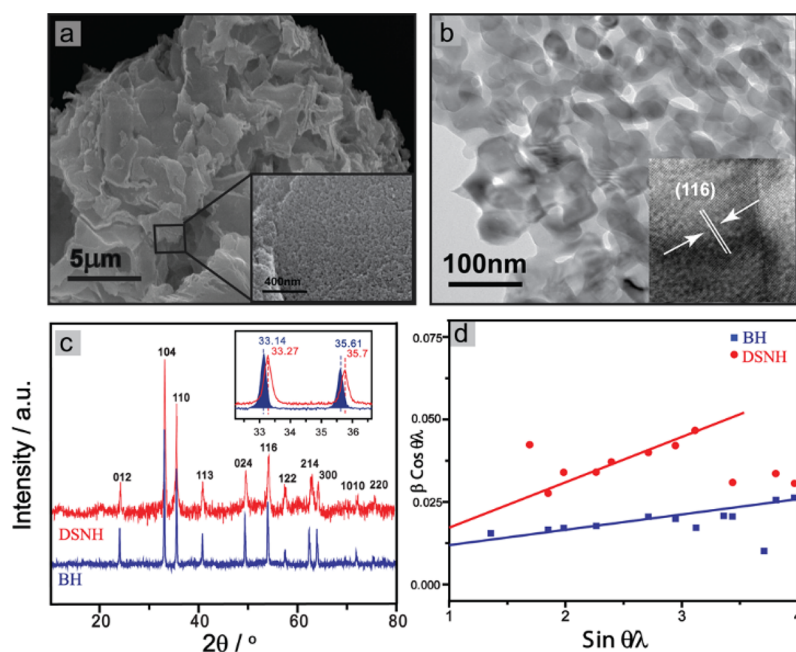
Figure 1. FE-SEM images of (a) DSNH materials obtained by pyrolyzing aerogel at 500 °C. The inset shows the mesoporous structure of DSNH. (b) Highly interconnected network in DSNH as seen via HRTEM and (c) PXRD pattern comparing DSNH with BH. Inset shows the fwhm broadening and shift in the pattern toward higher 2θ in DSNH because of the strain induced by the defect, and (d) strain induced in DSNH and BH was calculated using Williamson–Hall measurement.
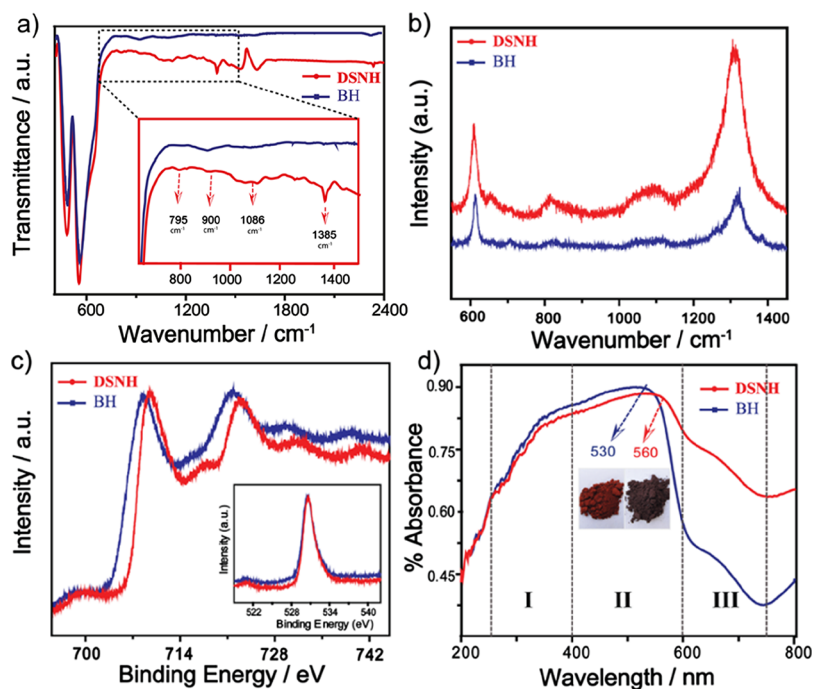

Figure 2. (a) IR–vis spectra of DSNH and BH. The inset shows the vibration modes of 795 cm^{-1} of Fe–O–H out-of-plane deformation, 900 cm^{-1}—Fe–O–H bending vibrations, 1086 cm^{-1}—α-FeOOH, and 1385 cm^{-1}—metal coordinated CO$_3^-$ modes present in DSNH, whereas these modes are absent in BH. (b) Raman spectra reveals the defect mode present at 660 cm^{-1} in DSNH and not in BH. (c) Fe 2p core level XPS spectra of DSNH and BH. The inset shows the O 2p core level spectra. (d) UV–vis spectra of DSNH showing red shift at 560 cm^{-1} as compared to that of BH at 530 cm^{-1} and increased intensity in region III.

space group of the corundum structure. As shown in the inset, the full width at half-maximum (fwhm) of the main peak for DSNH is broader than that for BH, which implies much smaller grain size with the possible presence of defects. The PXRD patterns were refined using multiprofile Rietveld refinements (Figure S1 in the Supporting Information), which showed

anisotropic dilation in the cell volume of DSNH (298.24 Å^3) with reference to that of BH (297.08 Å^3) because of the iron vacancy (V_{FE}), as revealed by the formula sum of Fe$_{11.472}$O$_{18.002}$ with an iron occupancy of 0.956 and oxygen being 1. Hence, a discrepancy is noted in the Fe–O (1.930 Å) and O–O (2.110 Å) bond lengths agreeing with previous studies[21] (Table S1 in
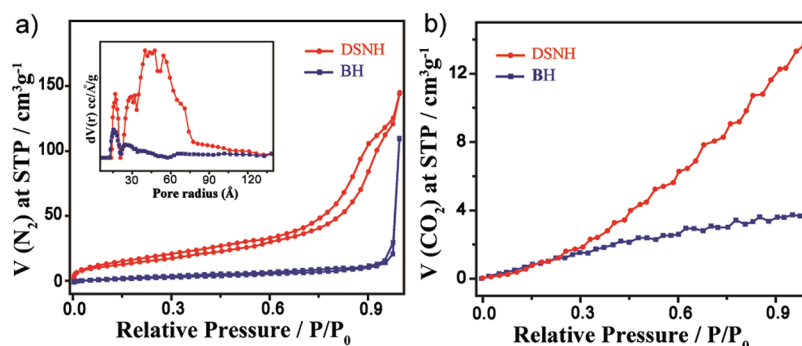
Figure 3. (a) N_2 adsorption/desorption isotherms of DSNH and BH recorded at 77 K, and the inset shows their pore size distribution calculated from the isotherms. (b) CO_2 adsorption isotherms at 273 K for DSNH and BH.

the Supporting Information), which implies the existence of the nonstoichiometric metastable phase of hematite in the DSNH case. This is similar to the protohematite phase, as reported by Gualtieri et al.[22] The presence of such a defect phase also induces strain, which can be inferred from the Williamson−Hall analysis (Figure 1d) which clearly shows the significant difference between the strain states of DSNH and BH samples. Because the defect-induced changes in XRD parameters are always very small, we employed a few other key techniques to elucidate the differences between the DSNH and BH materials further.

First, the technique of infrared (IR) spectroscopy is employed, and the corresponding data are shown in Figure 2a. The very strong IR bands at 460 and 544 cm^{-1} belong to the Fe−O stretching and bending modes of pure hematite, respectively, and the intense 645 cm^{-1} feature can be ascribed to the Fe−O stretching vibration. The key features observed at 795 and 900 cm^{-1} are assigned to the out-of-plane deformational (g) modes of hydroxyls, which can be ascribed to the Fe−O−H bending vibration. The presence of these distinctive peaks implies that DSNH has a defect-stabilized Fe−O$^-$ matrix, which upon atmospheric adsorption of moisture can show the fingerprint Fe−O−H signatures. It may be noted that these are mostly absent in the case of BH. The next prominent mode, a broad multiline spectrum at around 1086 cm^{-1}, can be assigned to the fingerprint region as in α-FeOOH.[23,24] Moreover, the absorption at 1385 cm^{-1} originates from the monodentate CO_3^- formation due to the adsorption of atmospheric CO_2.

Raman spectra recorded to elucidate the finer features of the microstate of the sample and reveal the enhanced contribution at 660 cm^{-1} in DSNH with reference to the BH sample (Figures 2b and S2 in the Supporting Information). The second overtone of the 660 cm^{-1} mode, located at 1320 cm^{-1}, is also clearly and substantially enhanced in the DSNH case. The increased intensity in two-phonon scattering at 1300 cm^{-1} can be assigned to the second-order scattering process. A reasonable interpretation for the enhancement of the 660 cm^{-1} mode, which is a Raman forbidden LO Eu mode, is the disorder-induced symmetry breaking caused by the metastable defect states in DSNH; notably, this 660 cm^{-1} mode is inactive in BH as expected.

We also applied X-ray photoelectron spectroscopy (XPS) to elucidate the differences in the nature of surface layers of DSNH and BH (Figures 2c and S3 in the Supporting Information). It is observed that in DSNH, the Fe 2p core level line position has shifted considerably (almost 1.1 eV) toward higher binding energy as compared with BH. The shift toward the higher energy results from the withdrawal of the

electron density. An iron vacancy V_{Fe}, if present, would impart the neighboring oxygen with a high electron density which in turn would further get surface hydroxylated. Thus, the electron density on the Fe neighbors will be withdrawn, which is reflected in the shift of the Fe 2p core level toward higher energy.

The diffuse reflectance spectroscopy (DRS) data shown in Figures 2d and S4 in the Supporting Information reveal that the absorption maximum of the BH material is at 530 nm and that of DSNH is at 560 nm, reflecting a red shift. A typical absorption spectrum of hematite has four absorption regions. In particular, the absorbance in region III (600−780 nm) corresponds to the $^6A_1(^6S)$ to $^4T_2(^4G)$ ligand field transition at about 640 nm. In the DSNH case, region 3 is very prominent with increased intensity unveiling the increased ligand field transitions; the absorption intensities of which are partially derived from the orbital mixing between Fe^{3+} and O^{2-} ions. Iron vacancies in DSNH increase the surface charge density of oxygen ions, thereby affecting the electronic and spin properties of Fe^{3+} under the influence of ligand field provided by the oxygen ions.[25] The displacement of the equilibrium lattice geometry upon $^6A_1(^6S)$ to $^4T_2(^4G)$ excitation creates coherent phonons, and the effect is pronounced in nanocrystals as seen for the DSNH sample.

The pore size distribution and surface area of both the DSNH and BH samples were examined by using N_2 adsorption isotherms at 77 K (Figure 3a). A typical type-VI reversible isotherm behavior is exhibited by DSNH, which is the characteristic feature of mesoporous materials, whereas the BH sample follows a typical type-II reversible isotherm behavior. The Brunauer−Emmet−Teller surface area was found to be 53 $m^2 g^{-1}$ and 12 $m^2 g^{-1}$ for the DSNH and BH samples, respectively. The significant increase in the surface area clearly indicates the particle size reduction and possibility of the presence of more active adsorptive sites on the DSNH surface. The half pore size distribution of BH (inset of Figure 3a) was found to be 1.0−2.0 nm and that of DSNH covered a wide range between 1.0 and 9.0 nm. This very well encompasses the mesoporous region. Arguably, DSNH should ideally show high CO_2 uptake because of the presence of reactive DSNH, and this motivated us to explore its efficacy for CO_2 adsorption. The CO_2 uptake values for BH and DSNH were found to be 3.6 $cm^3 g^{-1}$ and 13.6 $cm^3 g^{-1}$, respectively, at 273 K and 1 atm (Figure 3b). The increased CO_2 uptake by DSNH can be attributed to the presence of defect-stabilized sites in hematite that interact effectively with CO_2.

Further, the presence of defects was corroborated by magnetization studies, as shown in Figure S5 in the Supporting
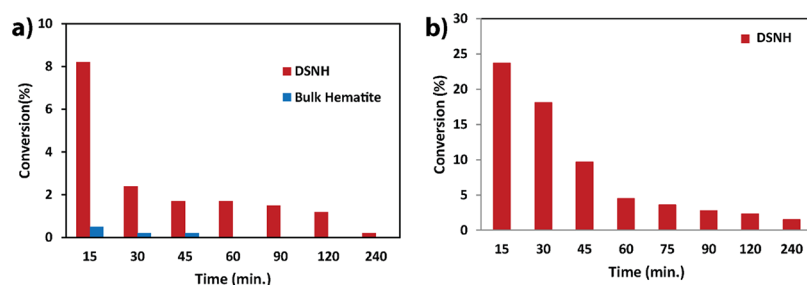
Figure 4. Conversion of CO_2 over DSNH: (a) CO_2 conversion over DSNH and BH at RT over a period of time and (b) CO_2 conversion over DSNH at 300 °C over a period of time.

Information. The presence of specific defects, disorder, microstructure, and shape can influence the remanence and coercive field of this component significantly. In our case, it can be seen that the values of remanence (coercive field) for the BH and DSNH samples are 0.74 emu/g (924.7 Oe) and 0.83 emu/g (2821.9 Oe), respectively. The higher value of remanence and a significantly high value of coercive field in the case of DSNH as compared to that of BH can be attributed to the magnetocrystalline anisotropy effect due to the peculiar interbraided shape character of DSNH as shown by the TEM images (Figure 1b), as well as the presence of defects as brought out by other techniques.

The transmission Mössbauer spectra for DSNH and BH samples are shown in Figure S6a,b in the Supprting Information, along with the fitted component(s). The corresponding hyperfine interaction parameters (Table S2 in the Supporting Information) show a major contribution of the magnetic sextet characteristic of hematite, as expected. However, in the DSNH case, a tiny (1.7%) yet unmistakable contribution of a quadrupole-split doublet (nonmagnetic contribution) is also noted. The isomer shift (IS) of the doublet is 0.205 mm/s, which represents Fe in the Fe^{3+} state, but the corresponding value is lower than the characteristic IS for the α-Fe_2O_3 phase ($\sim$0.37 mm/s). Additionally, the sign of the quadrupole splitting for the doublet is opposite to that of the base hematite phase. Such a doublet can arise due to the presence of adsorbed moisture on the reactive Fe−O^- within the DSNH matrix and thus represents the fingerprint region similar to ferrihydrite as discussed in the IR section (Figure 2a). This points to the signature of a defect state in the basic matrix. It may also be noted that the line widths of the fitted components in the DSNH case ($\sim$0.16 mm/s) are slightly larger than that for the BH case. This can be due to defects and related matrix strain.

The formation of CO from CO_2 on DSNH was investigated in a stainless steel flow reactor at RT, and the results are shown in Figure 4. Initially, Ar was passed through the material to ensure that there are no carbon remnants present in the same which could contribute to the CO_2 reduction to CO, and no CO was recorded in the gas chromatography (GC). Later, a fresh sample was used for further studies. At 15 min, a maximum CO formation rate of 410 μmol h^{-1} g^{-1} was observed for DSNH, whereas BH showed a negligible rate of 10 μmol h^{-1} g^{-1}. On DSNH, the CO_2 conversion at 15 min was found to be 8.1%. This remarkable increase in the formation of CO can be attributed to the active defect sites present only in the case of our DSNH sample surface. At 30 min, the CO conversion rate decreased to 2.8%. The activity was found to be negligible beyond 240 min. We also studied DSNH at 300 °C in the stream of CO_2, and the initial conversion of CO_2 to CO

was seen to increase significantly by three times as compared to that at RT. Although the trend of deactivation was similar to that at RT, it occurred at a slower rate at 300 °C.

We examined DSNH before and after CO_2 addition by employing IR-vibrational spectroscopy (Figure 5) and XPS
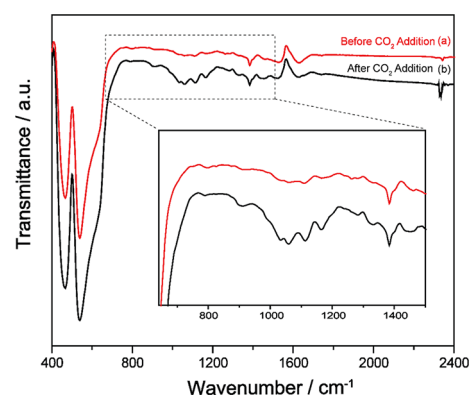

Figure 5. The IR−vis spectra were obtained for DSNH (a) before addition of CO_2 and (b) after addition of CO_2.

(Figure S8 in the Supporting Information). As discussed earlier (Figure 2a), the bands at 795 and 900 cm^{-1} in DSNH before CO_2 addition are due to Fe−OH deformational modes. A broad multiline band noted in the range of 1000−1350 cm^{-1} represents α-FeOOH-like atomic coordination attributable to the defect modes. Interestingly, upon the addition of CO_2, these contributions are concomitantly and significantly enhanced in the range of 1000−1350 cm^{-1} identified with the surface oxidation of DSNH, leading to the increased concentration of α-FeOOH. This suggests that the incoming CO_2 interacts with the active surface defects Fe−O^- in DSNH forming variety of intermediate CO_2 species such as gas-phase CO_2^-, chemisorbed CO_3^-, and Fe−CO_3^-. The presence of both the activated CO_2^- in the gas phase and the chemisorbed CO_3^- species was further corroborated by C 1s core level XPS spectra (Figure S8 in the Supporting Information).

RT activation of CO_2 to CO on DSNH, which intrinsically requires a higher energy (ΔG_{1000K} = 190.5 kJ mol^{-1}), is a significant discovery reported in this work. The presence of oxide vacancies has been known to activate CO_2 at RT under dark conditions.[26] In the case of DSNH, there are two important observations that support the participation of Fe vacant sites (V_{Fe}). First, a rapid deactivation of the material observed with the conversion almost dropping to zero within a period of 4 h. Second, the Fourier transform infrared (FT-IR) spectra of the used DSNH samples show a significant increase in the bands corresponding to the −OH groups of
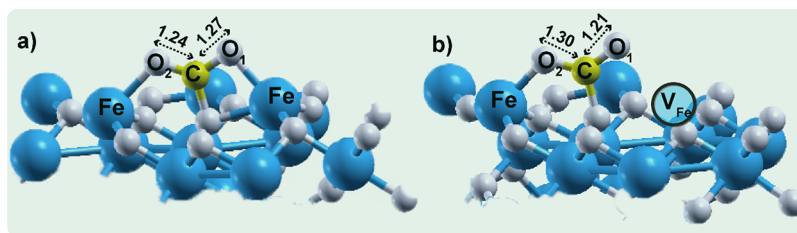
Figure 6. CO_3^- carbonate-like structures formed at (a) pristine and (b) defect V_{Fe} Fe_2O_3 surface. The bond lengths are given in Å (Fe = blue, O = white, and C = yellow).

oxohydroxide phases (Figure S9 in the Supprting Information). It is plausible that V_{Fe} defects in DSNH are capable of chemisorbing CO_2 as surface carbonate because of the increased basicity of oxide ions (surrounding the V_{Fe} site) which spontaneously decompose to CO accompanied by the Fe−O bond formation. Hydroxylation of Fe−O by atmospheric moisture is traced using FT-IR (Figure S9 in the Supporting Information) for the used DSNH. More importantly, the reason for rapid deactivation seems to be due to the progressive hydroxylation of Fe atoms probably adjacent to V_{Fe} sites, leaving behind the undecomposed surface CO_3^{2-} blocking the active site V_{Fe}. Importantly, heating the used deactivated DSNH to 500 °C for 3 h regained its activity up to 60−80%.

The absence of a carbon source before exposing the material to CO_2 environment was confirmed by the thermogravimetric analysis (TGA) profile, revealing that the product formed is solely by CO_2 passed through the material externally (Figure S11in the Supporting Information). In the case of DSNH, after CO_2 reduction, a slow degradation pattern is observed up to 300 °C with 5% weight loss that can be attributed to the presence of OH groups on the material surface. Further steep degradation at 370 °C with 8.8% weight loss of carbon present in the system confirms that there are some stable intermediate adducts such as CO_3^- on the sample surface, supporting the FT-IR studies. The recyclability tests on DSNH at RT were conducted for five successive cycles which reveals that the conversion ability is retained but decreased significantly down to 3% (Figure S12 in the Supporting Information).

We attempted to elucidate the surface mechanisms discussed above with the help of computer modeling studies. All DFT calculations were carried out with the Vienna Ab initio Simulation Package[27,28] at the generalized gradient approximation level. Ion−electron interaction was described by the projector augmented wave[29] pseudopotential with the Perdew−Burke−Ernzerhof[30] functional as the exchange−correlation functional of the electrons. Spin polarization was applied for all calculations. An energy cutoff of 520 eV was used for the plane-wave basis set. The Fe_2O_3 (0001) surface was presented by a layered slab. A 2 × 2 supercell along z-direction with a vacuum layer of 20 Å was used. The system contained 120 atoms, and only the gamma-point was used for the sampling of Brillouin zone. The structures were optimized until the maximum force on the atoms was less than 0.005 eV/Å.

The adsorption energy of CO_2 on the pristine and defective surfaces was calculated by the following equation

$$E_{ads} = E_{CO_2+surface} - E_{CO_2} - E_{surface}$$

The DFT results showed that the Fe vacancy indeed plays an important role in the CO_2 adsorption. The adsorption of CO_2 on the pristine and defective Fe_2O_3 surface is in the form of the CO_3^- carbonate-like structure[31] (Figure 6). This CO_3^-

carbonate configuration is in conformity with the IR spectra (the observed frequency at 1385 cm^{-1}). The C−O bond length is 1.18 Å in the gas-phase CO_2 molecule. In pristine Fe_2O_3 surface, the C=O bond length increases from 1.18 to 1.24 Å. However, in the case of defect V_{Fe} Fe_2O_3 surface (DSNH case), the asymmetrical stretch in the C=O bond length is 1.30 Å. Thus, because of the Fe vacancy, the C−O bond elongation increases from 1.24 to 1.30 Å. The adsorption energy of CO_2 on the defective Fe_2O_3 surface is 1.62 eV. In the case on dissociation of CO_2, oxygen vacancy plays a vital role,[31,32] which is also borne out in our case. The conversion of CO_2 to CO is possible if the reduced Fe_2O_3 surface is oxidized and desorption of CO occurs. This process is also energetically favorable, as shown in Figure 7.

■ CONCLUSIONS

In conclusion, we have synthesized a dual DSNH material by utilizing the MOF-100 gel which can enable the RT activation and conversion of CO_2 to CO. Indeed, we realized a highly enhanced output of 410 μmol h^{-1} g^{-1} at RT, as compared to that of 10 μmol h^{-1} g^{-1} for BH. The progressive deactivation of this DSNH material is correlated with the hydroxylation of the surface. It is argued based on the activity degradation under cycling and first principles DFT calculations that concurrent presence of nearby vacancies of Fe and O on the surface is essential for this energetically unfavorable process to occur at RT, and the excess chemical energy embedded in the defect-stabilized surface is expended in this high-energy conversion process, which leads to progressive filling up of oxygen vacancies.

■ EXPERIMENTAL SECTION

Materials and Synthesis. All reagents and solvents used for the synthesis and analysis were commercially available and used as received. Bulk α-Fe_2O_3 was purchased from Alfa Aesar. Iron nitrate was purchased from Merck, ethanol was purchased from Analytical Reagents, and trimesic acid was purchased from Sigma-Aldrich and was used without further purification unless otherwise noted.

Synthesis of MOF-100. The detailed synthetic procedure for the synthesis of metallogel MOF-100 was followed as reported previously.[33] In a typical reaction, 0.8 g (0.2 M) of trimesic acid was dissolved in 20 mL of ethanol and 2.4 g (0.3 M) of ferric nitrate was dissolved again in 20 mL of ethanol. The above two solutions were mixed together under vigorous stirring at RT to form MOF-100 gel instantaneously.

Synthesis of DSNH. The above-synthesized gel was allowed to set overnight at RT. The so-obtained gel was freeze-dried to remove the solvent for 2 days. The free flowing gel powder was heated under atmospheric conditions initially at the rate of 2° min^{-1} up to 250 °C for 2 h, cooled down to RT,
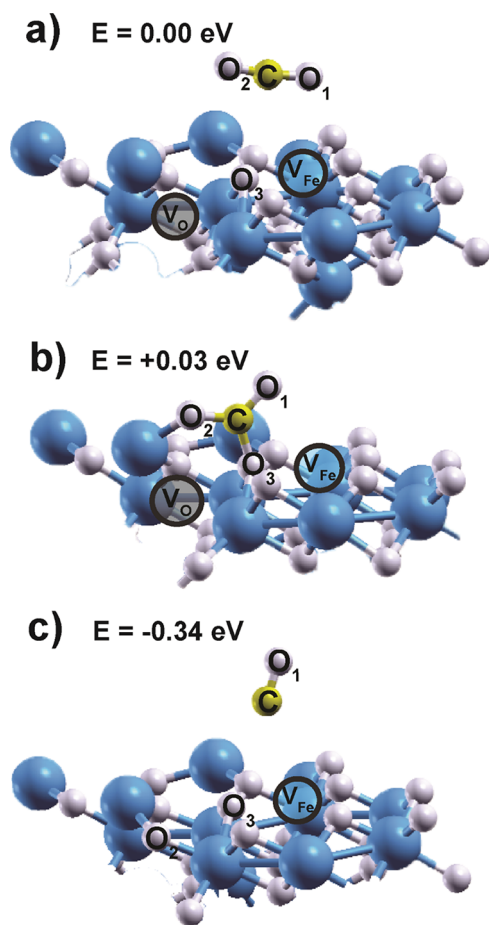
Figure 7. Energetics of adsorption and dissociation of CO_2 as influenced by the iron (V_{Fe}) and oxygen (V_O) vacancies (Fe = blue, O = white, C = yellow, and O_v = red) based on DFT calculations: (a) CO_2 adsorption on iron (V_{Fe}) and oxygen (V_O) vacant defect Fe_2O_3, (b) CO_3^- carbonate-like intermediate formation on iron (V_{Fe}) and oxygen (V_O) vacant defect Fe_2O_3, and (c) dissociation of CO by filling the V_O site by the oxygen from CO_2.

and again re-heated in air at the rate of 2° min^{-1} up to 500 °C for 3 h to obtain DSNH.

Characterization Techniques. The PXRD analysis of the DSNH and BH was carried out on a Philips PANalytical diffractometer in the reflection mode using Cu Kα radiation (λ = 1.540 Å). The 2θ range was scanned from 10° to 80° with a scan rate of 2.5° min^{-1}. Surface morphological features were examined using high-resolution transmission electron microscopy (HRTEM, FEI Techai F30 with 300 kV FEG). The TEM samples were prepared by drop-casting the sample dispersed in isopropanol on copper grids (TED PELLA Inc, 200 mesh). The scanning electron microscopy (SEM) images were obtained with Zeiss DSM-950 SEM and FEI Quanta 200 3D SEM with a tungsten filament as an electron source operated at 10 kV. The surface oxidation states were analyzed by XPS (VG scientific ESCA-3000 spectrometer) using non-monocromatized Mg Kα radiation (1253 eV) at a pressure of ~1 × 10^{-9} Torr. All gas adsorption experiments (up to 1 bar) were performed on a Quantachrome QUADRASORB automatic volumetric instrument. The molecular vibrations were confirmed by Raman spectroscopy using a LabRAM HR800 instrument from JY Horiba. The ultraviolet−visible (UV−vis) DRS were recorded using a LAMBDA-950 PerkinElmer

spectrophotometer in the wavelength range from 200 to 800 nm. FT-IR spectra were recorded at ambient temperature on a PerkinElmer spectrum GX spectrophotometer. The magnetism measurements were performed on a SQUID VSM magnetometer (Quantum Design). Mössbauer analysis was performed using a 57 Co (Rh) γ-ray source and α-Fe foil as the standard for calibration. TGA experiments were carried out in the temperature range of 20−900 °C on a SDT Q600 TG-DTA analyzer under air atmosphere at a heating rate of 10 °C min^{-1}.

Techniques Used for the Study of Dissociation of CO_2 to CO and Product Identification. Dissociation of CO_2 was carried out in a long quartz tube reactor. Hundred milligrams of the sample was loaded in the reactor tube. The CO_2 gas with a flow rate of 2 mL min^{-1} (CO_2 > 99.995%) pass through the reactor. The flow rate of CO_2 was controlled using an Alicat MFC instrument (MC-100SCCM-D). The gaseous products passed through an ice-cooled trap to condense the moisture formed in the reaction before injecting to an online gas chromatograph (Nucon 5765 GC). The gases were analyzed with a Porapak-Q packed column attached to the flame ionization detector (FID) methanizer for the detection of CO, CO_2, and CH_4 and a HP-PLOT Q capillary column attached to FID for the detection of hydrocarbon. The conversion is reported as mol % determined by dividing the total carbon mole converted as the product to the carbon mole injected as CO_2 and the selectivity as the mole fraction to the total number of carbon moles produced as products.

■ ASSOCIATED CONTENT

Ⓢ Supporting Information

The Supporting Information is available free of charge on the ACS Publications website at DOI: 10.1021/acsomega.7b01505.

Schematic synthesis of DSNH, Rietveld refinement powplot, complete details of Raman data, XPS, UVDRS, magnetic measurements, and Mössbauer spectroscopy. It also includes a schematic and a brief discussion about the mechanism involved in the defect formation in DSNH. Data discussing IR, PXRD, TGA after CO_2 conversion, and recyclability test are also included along with the tables containing parameters of Rietveld refinement and Mössbauer spectroscopy (PDF)

■ AUTHOR INFORMATION

Corresponding Authors

*E-mail: n.divya@ncl.res.in (D.N.).
*E-mail: nanodinesh@gmail.com (D.J.).
*E-mail: satishogale@iiserpune.ac.in (S.O.).

ORCID ⓘ

Satishchandra Ogale: 0000-0001-5593-9339

Notes

The authors declare no competing financial interest.

■ ACKNOWLEDGMENTS

■ REFERENCES

(1) D'Alessandro, D. M.; Smit, B.; Long, J. R. Carbon Dioxide Capture: Prospects for New Materials. *Angew. Chem., Int. Ed.* **2010**, *49*, 6058−6082.

(2) Fujishima, A.; Honda, K. Electrochemical Photolysis of Water at a Semiconductor Electrode. *Nature* **1972**, *238*, 37−38.

(3) Wang, W.; Wang, S.; Ma, X.; Gong, J. Recent Advances in Catalytic Hydrogenation of Carbon Dioxide. *Chem. Soc. Rev.* **2011**, *40*, 3703−3727.

(4) Ma, J.; Sun, N.; Zhang, X.; Zhao, N.; Xiao, F.; Wei, W.; Sun, Y. A Short Review of Catalysis for CO2 Conversion. *Catal. Today* **2009**, *148*, 221−231.

(5) Baiker, A. Utilization of Carbon Dioxide in Heterogeneous Catalytic Synthesis. *Appl. Organomet. Chem.* **2000**, *14*, 751−762.

(6) Chueh, W. C.; Falter, C.; Abbott, M.; Scipio, D.; Furler, P.; Haile, S. M.; Steinfeld, A. High-Flux Solar-Driven Thermochemical Dissociation of CO_2 and H_2O Using Nonstoichiometric Ceria. *Science* **2010**, *330*, 1797−1801.

(7) Lim, H.-K.; Shin, H.; Goddard, W. A.; Hwang, Y. J.; Min, B. K.; Kim, H. Embedding Covalency into Metal Catalysts for Efficient Electrochemical Conversion of CO2. *J. Am. Chem. Soc.* **2014**, *136*, 11355−11361.

(8) Frese, K. W. Electrochemical Reduction of CO_2 at Solid Electrodes. In *Electrochemical and Electrocatalytic Reactions of Carbon Dioxide*; Sullivan, B., Ed.; Elsevier, 1993; pp 145−216.

(9) Benson, E. E.; Kubiak, C. P.; Sathrum, A. J.; Smieja, J. M. Electrocatalytic and Homogeneous Approaches to Conversion of CO2 to Liquid Fuels. *Chem. Soc. Rev.* **2009**, *38*, 89−99.

(10) Freund, H.-J.; Roberts, M. W. Surface Chemistry of Carbon Dioxide. *Surf. Sci. Rep.* **1996**, *25*, 225−273.

(11) Busca, G.; Lorenzelli, V. Infrared Spectroscopic Identification of Species Arising from Reactive Adsorption of Carbon Oxides on Metal Oxide Surfaces. *Mater. Chem.* **1982**, *7*, 89−126.

(12) Fukuda, Y.; Toyoshima, I. AES and UPS Studies of CO and CO2 Adsorption on Mg and MgO. *Surf. Sci.* **1985**, *158*, 482−489.

(13) Tsami, A.; Grillo, F.; Bowker, M.; Nix, R. M. Model NSR Catalysts: Fabrication and Reactivity of Barium Oxide Layers on Cu(111). *Surf. Sci.* **2006**, *600*, 3403−3418.

(14) Copperthwaite, R. G.; Davies, P. R.; Morris, M. A.; Roberts, M. W.; Ryder, R. A. The Reactive Chemisorption of Carbon Dioxide at Magnesium and Copper Surfaces at Low Temperature. *Catal. Lett.* **1988**, *1*, 11−19.

(15) Berkó, A.; Solymosi, F. Effects of Potassium on the Chemisorption of CO2 and CO on the Pd(100) Surface. *Surf. Sci.* **1986**, *171*, L498−L502.

(16) Kiss, J.; Révész, K.; Solymosi, F. Photoelectron spectroscop1c Studies of the Adsorption of CO2 on Potassium-Promoted Rh(111) Surface. *Surf. Sci.* **1988**, *207*, 36−54.

(17) Liu, Z. M.; Zhou, Y.; Solymosi, F.; White, J. M. Spectroscopic Study of K-Induced Activation of CO2 on Pt(111). *Surf. Sci.* **1991**, *245*, 289−304.

(18) Toda, Y.; Hirayama, H.; Kuganathan, N.; Torrisi, A.; Sushko, P. V.; Hosono, H. Activation and Splitting of Carbon Dioxide on the Surface of an Inorganic Electride Material. *Nat. Commun.* **2013**, *4*, 2378.

(19) Ghuman, K. K.; Hoch, L. B.; Szymanski, P.; Loh, J. Y. Y.; Kherani, N. P.; El-Sayed, M. A.; Ozin, G. A.; Singh, C. V. Photoexcited Surface Frustrated Lewis Pairs for Heterogeneous Photocatalytic CO2 Reduction. *J. Am. Chem. Soc.* **2016**, *138*, 1206−1214.

(20) Liu, L.; Zhao, C.; Li, Y. Spontaneous Dissociation of CO2 to CO on Defective Surface of Cu(I)/TiO2−x Nanoparticles at Room Temperature. *J. Phys. Chem. C* **2012**, *116*, 7904−7912.

(21) Burgina, E. B.; Kustova, G. N.; Tsybulya, S. V.; Kryukova, G. N.; Litvak, G. S.; Isupova, L. A.; Sadykov, V. A. Structure of the Metastable Modification of iron(III) Oxide. *J. Struct. Chem.* **2000**, *41*, 396−402.

(22) Gualtieri, A. F.; Venturelli, P. In Situ Study of the Goethite-Hematite Phase Transformation by Real Time Synchrotron Powder Diffraction. *Am. Mineral.* **1999**, *84*, 895−904.

(23) Prasad, P. S. R.; Prasad, K. S.; Chaitanya, V. K.; Babu, E. V. S. S. K.; Sreedhar, B.; Murthy, S. R. In Situ FTIR Study on the Dehydration of Natural Goethite. *Asian J. Earth Sci.* **2006**, *27*, 503−511.

(24) Graciani, J.; Mudiyanselage, K.; Xu, F.; Baber, A. E.; Evans, J.; Senanayake, S. D.; Stacchiola, D. J.; Liu, P.; Hrbek, J.; Sanz, J. F.; Rodriguez, J. A. Highly Active Copper-Ceria and Copper-Ceria-Titania Catalysts for Methanol Synthesis from CO_2. *Science* **2014**, *345*, 546−550.

(25) Chen, T.-Y.; Hsia, C.-H.; Son, H. S.; Son, D. H. Ultrafast Energy Transfer and Strong Dynamic Non-Condon Effect on Ligand Field Transitions by Coherent Phonon in γ-Fe2O3 Nanocrystals. *J. Am. Chem. Soc.* **2007**, *129*, 10829−10836.

(26) Liu, L.; Zhao, C.; Li, Y. Spontaneous Dissociation of CO_2 to CO on Defective Surface of Cu(I)/$TiO_{2−X}$ Nanoparticles at Room Temperature. *J. Phys. Chem. C* **2012**, *116*, 7904−7912.

(27) Kresse, G.; Furthmüller, J. Efficiency of Ab-Initio Total Energy Calculations for Metals and Semiconductors Using a Plane-Wave Basis Set. *Comput. Mater. Sci.* **1996**, *6*, 15−50.

(28) Kresse, G.; Furthmüller, J. Efficient Iterative Schemes for Ab Initio Total-Energy Calculations Using a Plane-Wave Basis Set. *Phys. Rev. B* **1996**, *54*, 11169−11186.

(29) Blöchl, P. E. Projector Augmented-Wave Method. *Phys. Rev. B* **1994**, *50*, 17953−17979.

(30) Perdew, J. P.; Burke, K.; Ernzerhof, M. Generalized Gradient Approximation Made Simple. *Phys. Rev. Lett.* **1996**, *77*, 3865−3868.

(31) Mino, L.; Spoto, G.; Ferrari, A. M. CO_2 Capture by TiO_2 Anatase Surfaces: A Combined DFT and FTIR Study. *J. Phys. Chem. C* **2014**, *118*, 25016−25026.

(32) Ji, Y.; Luo, Y. New Mechanism for Photocatalytic Reduction of CO_2 on the Anatase TiO_2(101) Surface: The Essential Role of Oxygen Vacancy. *J. Am. Chem. Soc.* **2016**, *138*, 15896−15902.

(33) Lohe, M. R.; Rose, M.; Kaskel, S. Metal−organic Framework (MOF) Aerogels with High Micro- and Macroporosity. *Chem. Commun.* **2009**, 6056.